SATURATION AND POST-SATURATION BEHAVIOR OF THE ALFVÉN ION-CYCLOTRON INSTABILITY: A SIMULATION STUDY

by

Niels F. Otani

Memorandum No. M86/15

19 February 1986

SATURATION AND POST-SATURATION BEHAVIOR OF THE ALFVÉN ION-CYCLOTRON INSTABILITY: A SIMULATION STUDY

by

Niels F. Otani

Memorandum No. M86/15

19 February 1986

ELECTRONICS RESEARCH LABORATORY

College of Engineering
University of California, Berkeley
94720

SATURATION AND POST-SATURATION BEHAVIOR OF THE ALFVÉN ION-CYCLOTRON INSTABILITY: A SIMULATION STUDY

by

Niels F. Otani

Memorandum No. M86/15

19 February 1986

ELECTRONICS RESEARCH LABORATORY

College of Engineering
University of California, Berkeley
94720

Saturation and Post-Saturation Behavior of the Alfvén Ion-Cyclotron Instability: A Simulation Study

Niels F. Otani
Electronics Research Laboratory
University of California
Berkeley, California 94720

Two computer codes based on different algorithms are employed in the study of the Alfvén ion-cyclotron instability. Features of quasilinear diffusion are clearly exhibited and identically modeled by the two codes. Ion trapping is also observed and appears to play an important role in the saturation process. Relaxation of the anisotropy in the ion temperature and transverse wave energy transfer from intermediate to long wavelength modes are observed to proceed more slowly following instability saturation when the possibility of nonlinear $\mathbf{E} \times \mathbf{B}$ electrons is allowed, and more slowly still when longitudinal ion sound modes are present. Fluctuations in the short wavelength modes are shown to be a discrete particle effect, with levels agreeing with predictions calculated from a test-particle model.

I. INTRODUCTION

The Alfvén ion-cyclotron (AIC) instability is an important process in both space and experimental fusion plasmas. It is driven by a temperature anisotropy ($T_{i\perp}/T_{i\parallel} > 1$) in the ion velocity distribution. Evidence for its existence has recently been obtained in the local afternoon to dusk region of the Earth's magnetosphere by the geostationary satellite ATS-6 [1], and its existence in the magnetospheric ring current region has also been theorized [2]. The AIC instability was first observed in a laboratory in the tandem mirror experiment TMX at Livermore [3]. The instability played a role of considerable importance in the experiment, causing significant degradation of plasma confinement in the tandem mirror's central region [4-6].

Theoretical studies of both the linear [7,8] and quasilinear characteristics [9-11] of the AIC instability have been conducted by several researchers. In the linear regime, the instability is most unstable for propagation along the background magnetic field for wavenumbers in the vicinity of $k \sim O(\omega_{ci}/v_A)$. In the quasilinear regime, diffusion in ion velocity space occurs predominately in the region defined by $v_{\parallel} \approx (\omega - \omega_{ci})/k$, where ω and k take on the values of the frequencies and wavenumbers of the largest waves present.

Analysis of the nonlinear regime has been more difficult. Except for general theories predicting, for example, coupling of parallel-propagating Alfvén waves to longitudinal ion sound waves [9], theoretical study has been conducted primarily by means of computer simulation [11-14]. The computer studies display two common features: (1) the ion temperature anisotropy relaxes very rapidly as the instability saturates, and then continues to relax more slowly following saturation, and (2) field energy, found mainly in the most unstable modes at saturation, is observed to transfer slowly to the long-wavelength modes after saturation.

In this article, we report new results obtained from computer simulations of the AIC instability, and also make comparisons to previous simulations. Features of the linear and quasilinear behavior of the simulations are discussed in the context of existing theory and compared with other simulations. Post-saturation behavior of the instability is likewise compared with previous simulations with additional attention paid separately to the long, intermediate, and short wavelength modes after saturation. Three models are used for the electrons with differences noted. Finally, a fluctuation theory for parallel-propagating transverse waves is derived and applied to the analysis of the simulation results.

II. THE SIMULATION ALGORITHMS

Two simulation codes were used in the study. Both codes are based on algorithms similar to those described in Ref. 15. The codes are quasineutral, electromagnetic, assume

particle ions and fluid electrons, and ignore displacement currents. Although the two codes employ different algorithms, both model the same three equations,

$$\frac{d\mathbf{v}_i}{dt} = \frac{e}{m}\left(\mathbf{E} + \frac{\mathbf{v}_i \times \mathbf{B}}{c}\right), \qquad i = 1, \ldots, N, \tag{1}$$

$$\frac{\partial \mathbf{B}}{\partial t} = -c\nabla \times \mathbf{E}, \tag{2}$$

and

$$\nabla \times \mathbf{B} = \frac{4\pi}{c}(\mathbf{J}_i - ne\mathbf{u}_e), \tag{3}$$

and differ only in the way electrons are treated. One of the codes, TRACY, considers the electrons as a cold, linear $\mathbf{E} \times \mathbf{B}$ fluid,

$$ne\mathbf{u}_e = \frac{n_0 ec\mathbf{E} \times \mathbf{B}_0}{B_0^2}, \tag{4}$$

while the other code, named PEPSI, uses the inertialess electron momentum equation,

$$\mathbf{E} = -\frac{\mathbf{u}_e \times \mathbf{B}}{c} - \frac{T_e \nabla n}{en}, \tag{5}$$

where T_e, the electron temperature, is considered fixed. In these equations, $\mathbf{v}_i$ is the velocity of the i-th ion simulation particle, m is the ion mass, and $\mathbf{J}_i$ and $n = n_i = n_e$ are calculated from the ion particle current and number density respectively. Details of the TRACY algorithm may be found in Ref. 16 while the PEPSI algorithm is essentially the same as one used by Harned [17], differing only in its dimensionality (2 1/2-d, here run as a 1 2/2-d code) and its lack of provisions to treat low- and zero-density regions. All simulations for this study were conducted on a one-dimensional spatial grid aligned with a uniform background magnetic field $\mathbf{B}_0 = B_0\hat{\mathbf{z}}$ with periodic boundary conditions.

III. RESULTS

The two codes were used in three runs initialized with ion velocities chosen to model the ion distribution function [18]

$$f(v_\perp, v_\parallel) = \left(v_\perp^2 - v_h^2 - \frac{v_\parallel^2}{R-1}\right)^l H\left(v_\perp^2 - v_h^2 - \frac{v_\parallel^2}{R-1}\right) \exp(-\alpha_\parallel v_\parallel^2 - \alpha_\perp v_\perp^2), \tag{6}$$

typical of distributions found in mirror machines. Here $H(x)$ is the Heaviside step function. In these runs, $R = 1.5$, $l = 4$, $v_h^2/v_A^2 = 0.01875$, and $\alpha_\perp$ and $\alpha_\parallel$ were chosen so that $\beta_{i\perp} = 0.05$ and $\beta_{i\parallel} = 0.033$. These parameters are representative of trapped ion velocity distributions expected in an axicell version of MFTF-B, the tandem mirror experiment under construction at Livermore [8]. The three runs, here denoted as Run Nos. 1, 2, and 3, used respectively the TRACY code ($T_e = 0$), the PEPSI code with $T_e = 0$, and PEPSI

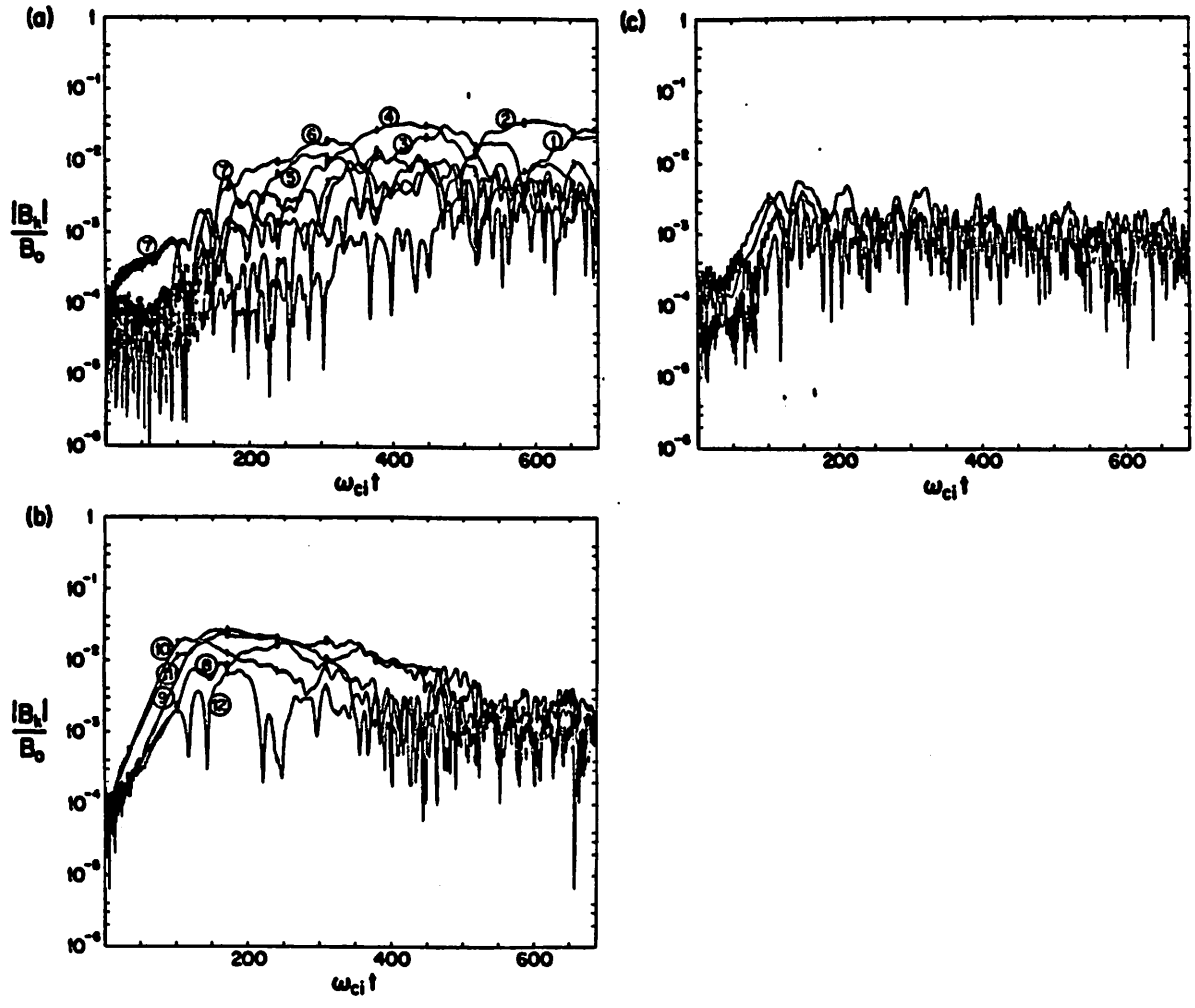

FIG. 1. Wave magnetic field mode amplitudes vs. time for Run No. 1 for (a) long wavelengths (modes 1–7, $0.20 \leq kv_A/\omega_{ci} \leq 1.39$), (b) intermediate wavelengths (modes 8–12, $1.59 \leq kv_A/\omega_{ci} \leq 2.38$), and (c) short wavelengths (modes 13–16, $2.58 \leq kv_A/\omega_{ci} \leq 3.18$).

with $(T_e/mv_A^2)^{1/2} = 0.45$. The simulations employed 10,000 particles and 256 grid-points with $\omega_{ci}\Delta t = 0.077$ and $v_A\Delta t/\Delta z = 0.62$, where $\omega_{ci} \equiv eB_0/mc$, $v_A \equiv (B_0^2/4\pi mn_0)^{1/2}$, and Δt and Δz are the timestep and grid spacing, respectively.

The runs were initialized in identical fashion with small perturbations in both the fields and the particle velocities. All runs displayed essentially identical diagnostics through the linear and quasilinear regimes up to wave saturation at $t \approx 150\omega_{ci}^{-1}$. Stability or clean linear growth through two orders of magnitude is observed for the long-wavelength modes (Figs. 1(a) and (b)) in agreement with theoretical linear growth rates calculated using G.

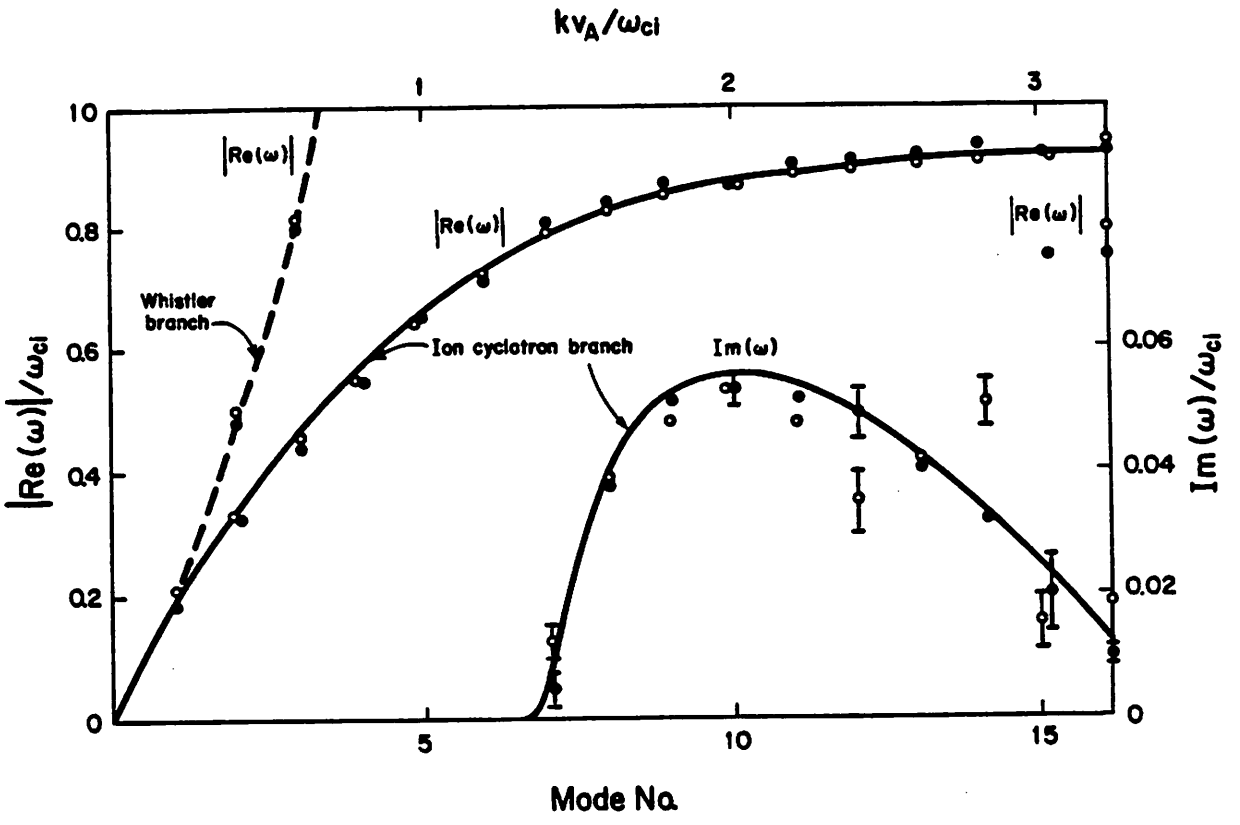

FIG. 2. Linear growth rates and principal mode frequencies obtained from TRACY for the mirror distribution function with $R = 1.5$, $l = 4$, $v_h^2/v_A^2 = 0.01875$, $\beta_{i\perp} = 0.033$, and $\beta_{i\parallel} = 0.05$ using 10,000 particles (open circles), or 100,000 particles (filled circles). The error bars on some of the growth rate data points reflect erratic growth on the part of the corresponding modes.

R. Smith's AIC dispersion solver [18]. Four or more decades of clean linear growth have been observed of similar modes in other simulations initialized with smaller perturbations. Mode frequencies at all wavelengths also agree well. Growth rates of the short-wavelength modes are, however, somewhat erratic (Fig. 1(c)) and generally differ from rates predicted by theory. Figure 2 compares the growth rates and mode frequencies obtained in these runs to an otherwise identical run employing 100,000 particles. The improved agreement of the short-wavelength growth rates with theory with the larger number of particles indicates that a discrete-particle effect is involved. A detailed discussion of this effect appears in a related paper [16].

Following the linear growth phase, the ion distribution of the three runs exhibits rapid velocity space transport in the vicinity of the resonant parallel velocities $v_\parallel = \pm(\omega - \omega_{ci})/k$. This effect is clearly displayed in Figs. 3(a) through (d). Diffusion in velocity space is

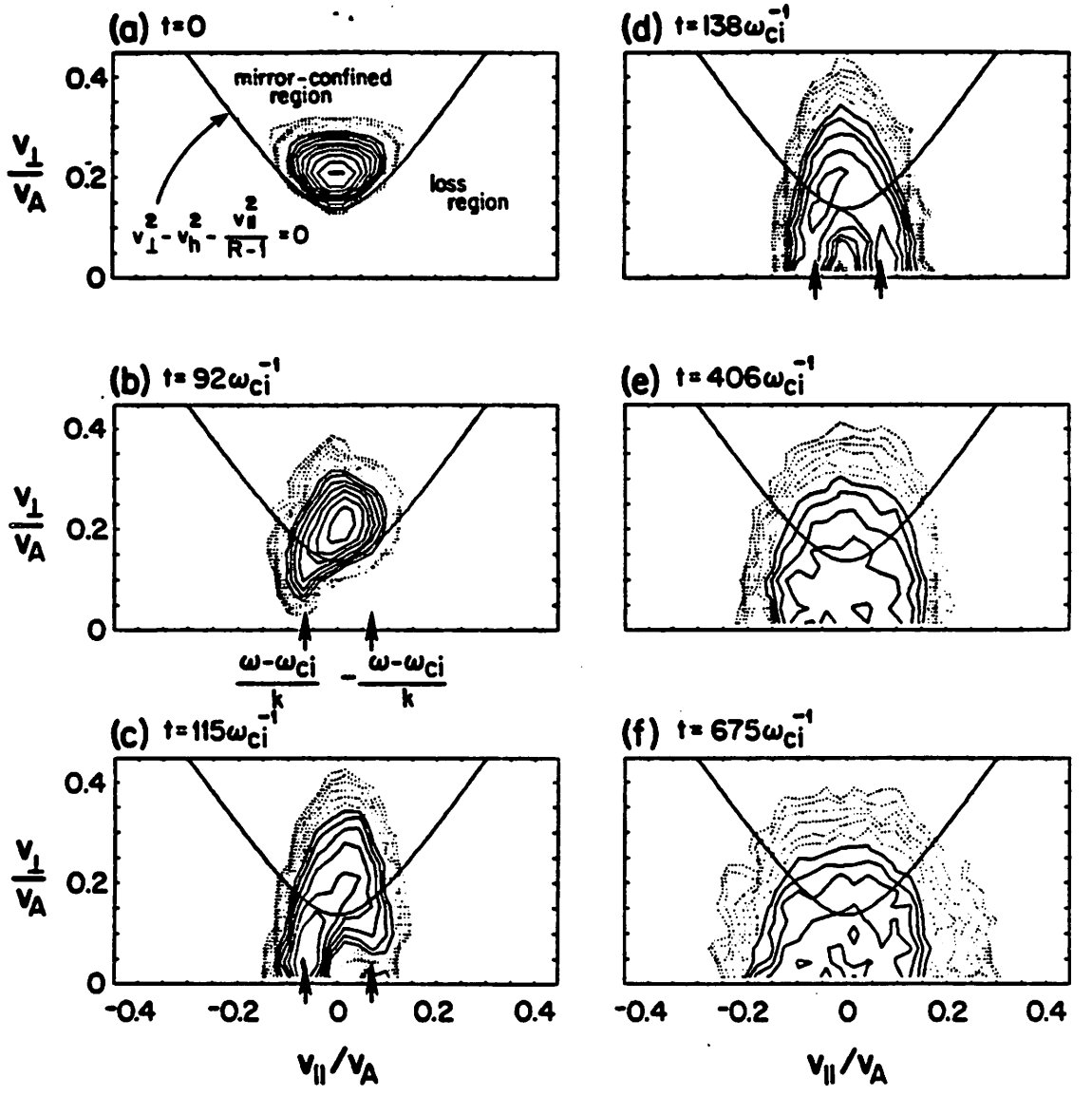

FIG. 3. Ion particle distribution contours in velocity space for Run No. 1 at times (a) $t = 0$, (b) $t = 92\omega_{ci}^{-1}$, (c) $t = 115\omega_{ci}^{-1}$, (d) $t = 138\omega_{ci}^{-1}$, (e) $t = 406\omega_{ci}^{-1}$, and (f) $t = 675\omega_{ci}^{-1}$. The contours are separated by factors of $\sqrt{2}$. The arrows indicate the resonant velocities for the linearly most unstable waves: $\omega = 0.87\omega_{ci}$, $k = \pm 1.99\omega_{ci}/v_A$.

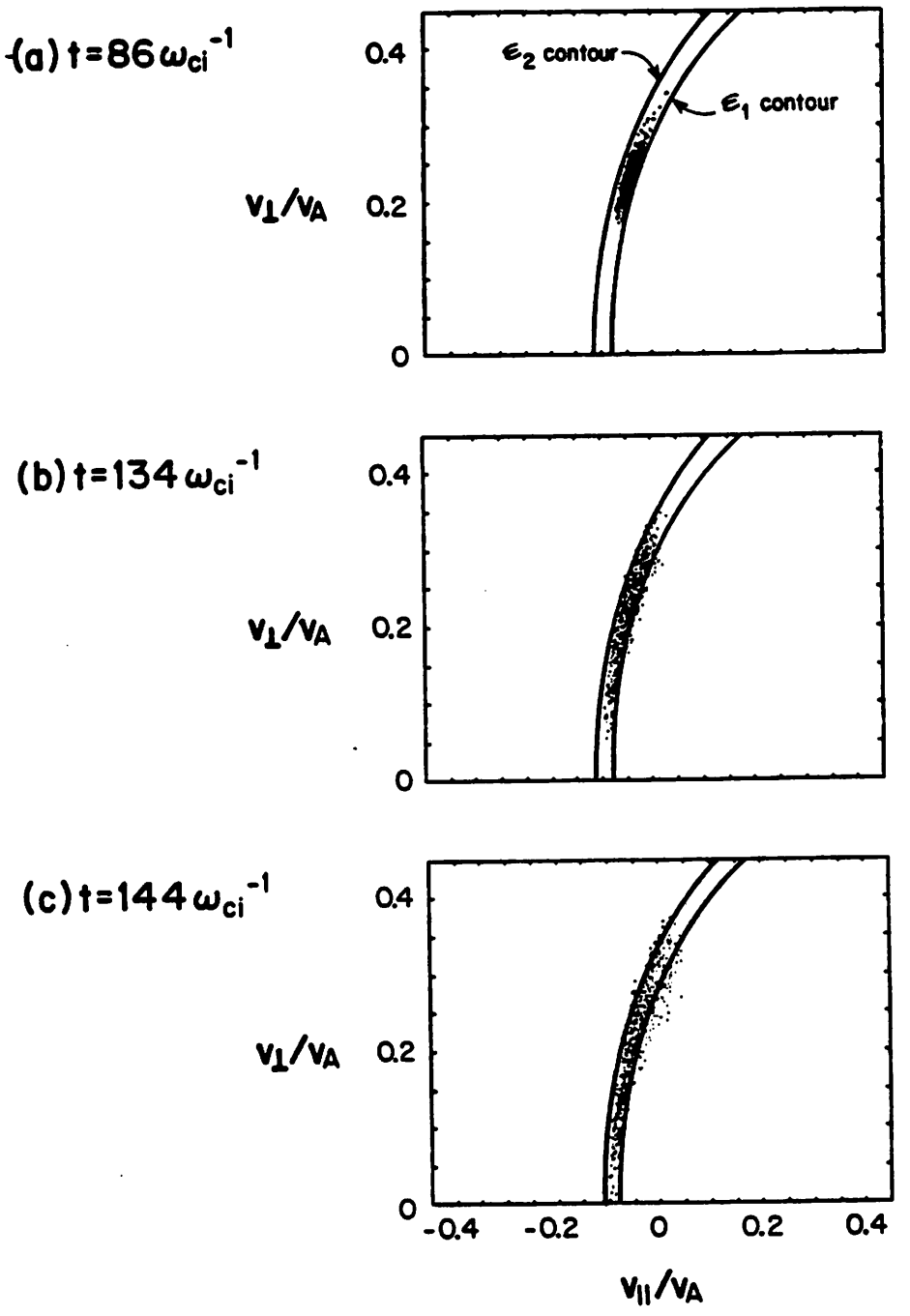

FIG. 4. Snapshots of ion particles loaded initially in the portion of the ion distribution between energies $\mathcal{E}_1 = 0.131 v_A^2$ and $\mathcal{E}_2 = 0.148 v_A^2$ in the wave frame defined by $\omega = 0.87\omega_{ci}$, $k = 1.99\omega_{ci}/v_A$, the linearly most unstable mode, at times (a) $t = 86\omega_{ci}^{-1}$, (b) $t = 134\omega_{ci}^{-1}$, and (c) $t = 144\omega_{ci}^{-1}$ for a run similar to Run No. 1 using 100,000 particles.

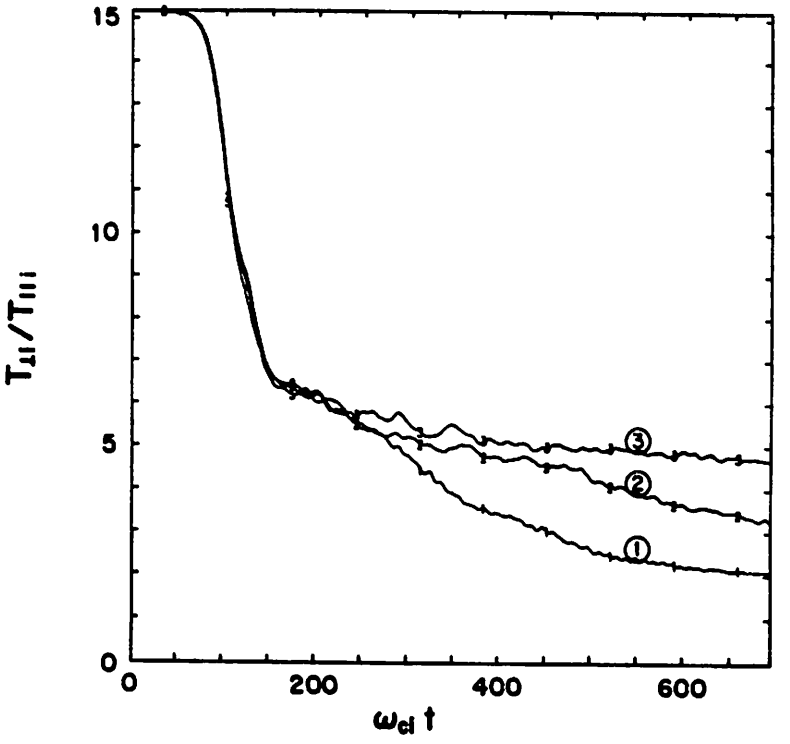

FIG. 5. $T_{i\perp}/T_{i\parallel}$ vs. time for Run Nos. 1, 2, and 3.

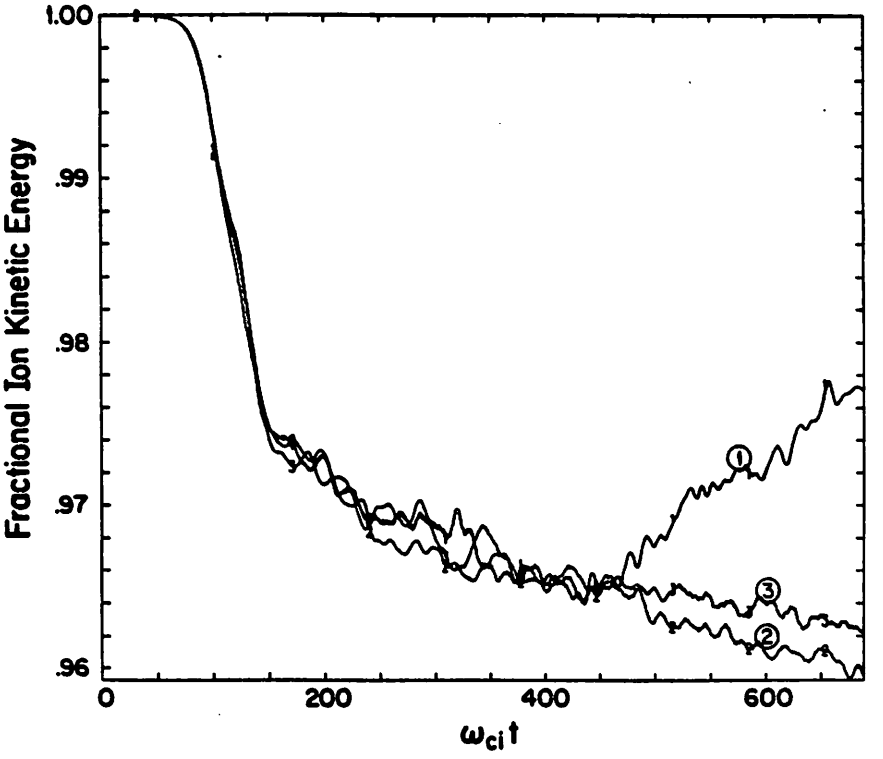

FIG. 6. Ion kinetic energy as a fraction of initial ion energy vs. time for Run Nos. 1, 2, and 3.

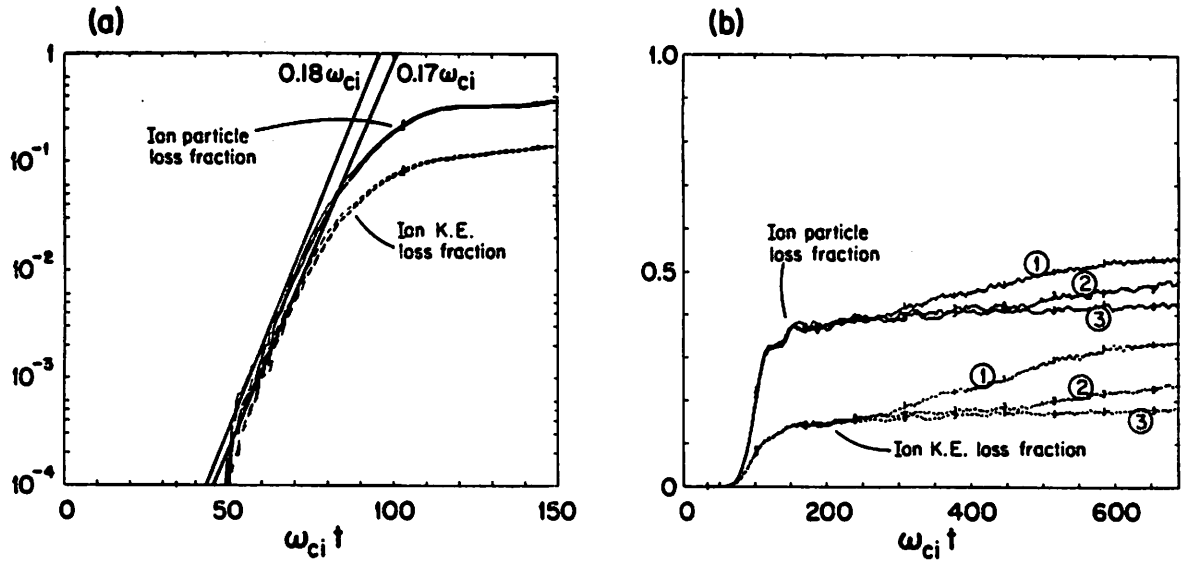

FIG. 7. Fraction of the total number of ions and total ion kinetic energy in the loss region $v_\perp^2 - v_h^2 - v_\parallel^2/(R-1) < 0$ as functions of time for Run Nos. 1, 2, and 3 for (a) $t < 150\omega_{ci}^{-1}$ and (b) the entire run.

observed to be directed along constant energy contours in the principal wave frame $v_\parallel = \omega/k$, as detailed in Fig. 4. Both the location and direction of velocity space diffusion thus agree with quasilinear theory. The nearly "vertical" transport observed in Fig. 4 is also consistent with the large relative change of perpendicular energy with parallel energy, $d\mathcal{E}_\perp/d\mathcal{E}_\parallel = \omega_{ci}/(\omega - \omega_{ci}) = -7.7$, predicted by quasilinear theory for resonant particles. In contrast, when the non-resonant particles are included, $d\mathcal{E}_\perp/d\mathcal{E}_\parallel \to -1.7$ as saturation occurs ($t < 140\omega_{ci}^{-1}$), which we find consistent with the relaxation of $T_{i\perp}/T_{i\parallel}$ from 15 to 6.5 (Fig. 5), the decrease of $\mathcal{E}_\perp$ by 6.4% (Fig. 6), the increase of field energy to 2.5% of the kinetic energy, and the conservation of total energy occurring over the same period. The apparent asymmetry between the two diffusion regions in Figs. 3(b) and (c) was caused by asymmetries in the initial perturbation. Particle and ion kinetic energy loss rates into the loss region have been measured for this simulation to be $0.18\omega_{ci}$ and $0.17\omega_{ci}$, respectively (Fig. 7(a)).

Definite departures from quasilinear theory are also observed in the pre-saturation phase. Although at saturation the regions of resonant trapping of many of the modes are well-overlapped (Fig. 8), characteristics of magnetic trapping are clearly visible in plots of selected particle trajectories (Fig. 9). Most of the trapping occurs about a gyrophase angle of $\psi = \pi$, where ψ is the angle between $\mathbf{v}_\perp$ and $\mathbf{B}_\perp(z)$, consistent with theories of parallel-propagating monochromatic electromagnetic waves [19,20]. Some trapping also

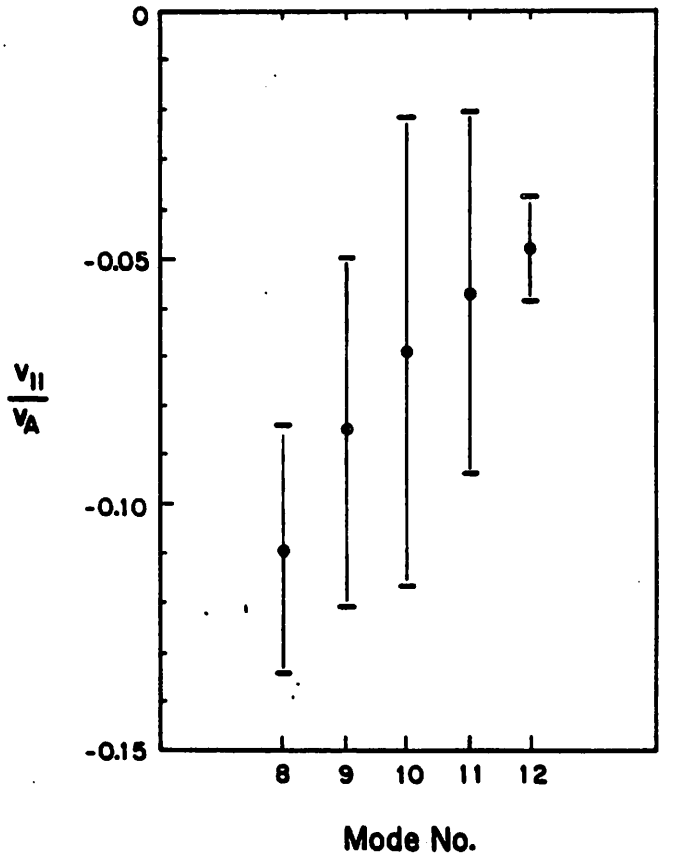

FIG. 8. Resonant trapping regions in parallel velocity space for modes 8–12 at mode 10 saturation ($t = 112\omega_{ci}^{-1}$) in Run No. 1. Each resonant region is computed from $(\omega - \omega_{ci})/k - v_t \leq v_{||} \leq (\omega - \omega_{ci})/k + v_t$, where ω is the theoretical linear mode frequency and v_t is the trapping velocity $(eB_k\langle v_\perp^2\rangle_i^{1/2}/mck)^{1/2}$ evaluated at $\omega_{ci}t = 112$.

occurs about $\psi = 0$ later in the run ($t > 130\omega_{ci}^{-1}$). Additionally, saturation of the most unstable mode (mode 10) occurs well before changes in the velocity distribution render it linearly stable. Saturation may instead occur by trapping, since the initial linear growth rate γ_0 is of order the trapping frequency ω_t at saturation (specifically, $\gamma_0/\omega_t = 0.26 \pm 0.05$). This possibility has been suggested by Ossakow *et al.* [14] in a similar study on the whistler instability, in which comparable values of γ_0/ω_t at saturation were obtained.

Evidence from other AIC simulations with TRACY supports the hypothesis that both quasilinear and trapping effects play important roles in the pre-saturation phase. Simulations following the evolution of an ion distribution initialized with a single value of $v_\perp$ under the influence of a single AIC-unstable mode display a number of distinctive characteristics including conservation of particle "helical" momentum and the appearance of a sharp "edge" in the ion velocity distribution function which is found associated with ion trapping

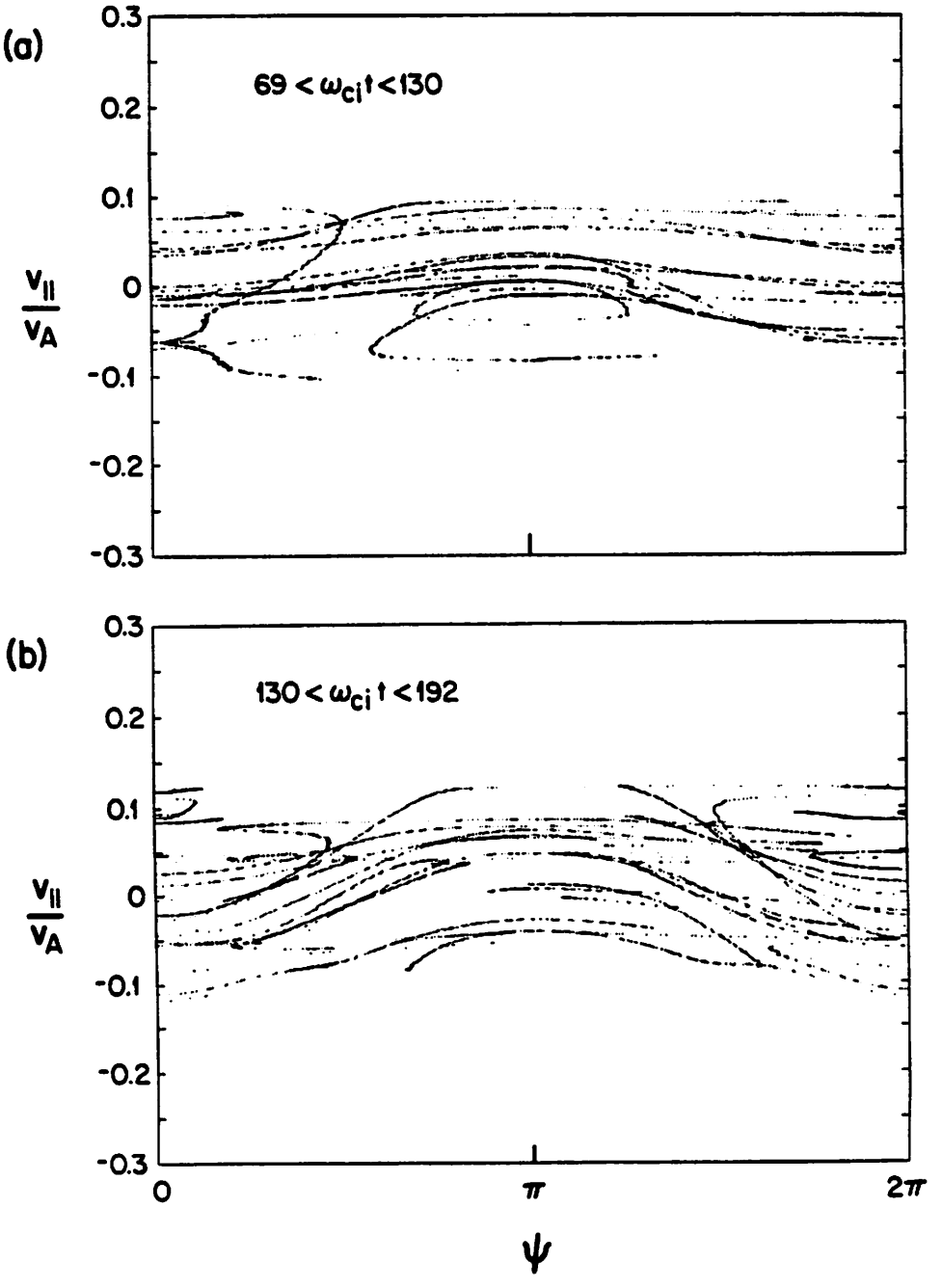

FIG. 9. Ten selected ion particle orbits in $v_{\|}$-ψ space from Run No. 1 for (a) $69 < \omega_{ci}t < 130$ and (b) $130 < \omega_{ci}t < 192$. Here ψ is the angle between $\mathbf{v}_{\perp}$ and $\mathbf{B}_{\perp}$. Points composing the orbits are spaced one timestep apart.

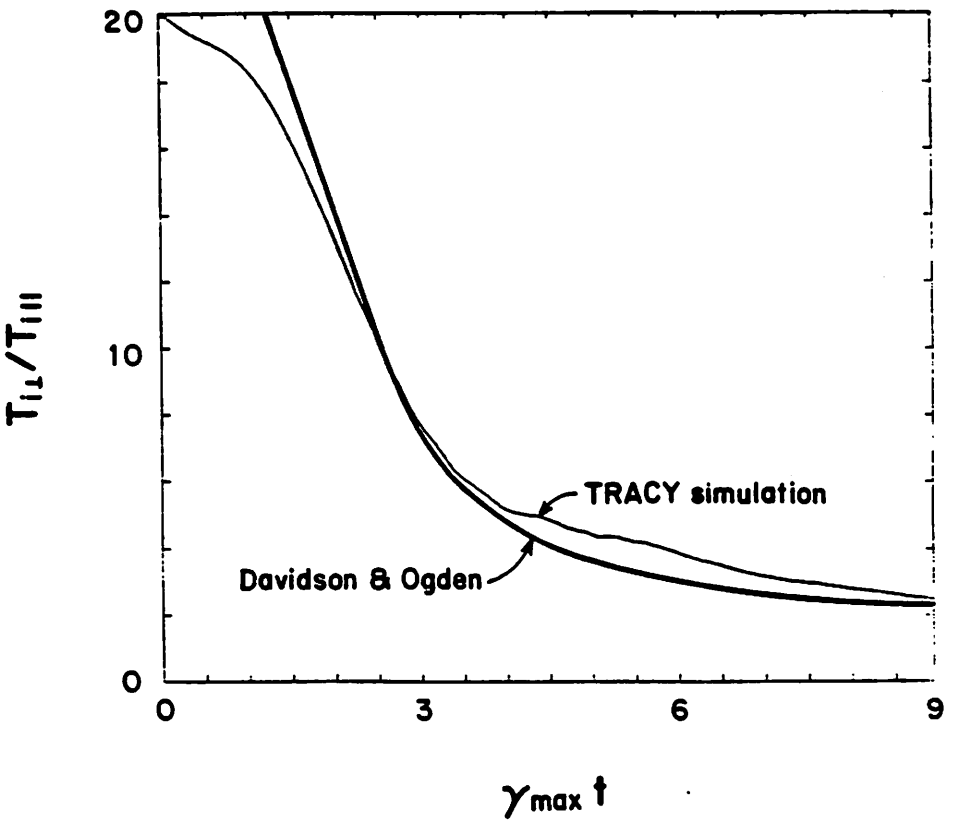

FIG. 10. Ion temperature anisotropy ($T_{i\perp}/T_{i\parallel}$) obtained from a TRACY simulation run, and as calculated numerically by Davidson and Ogden [10] using time-dependent quasilinear equations. Initial conditions for both runs were $T_{i\perp}/T_{i\parallel} = 20$ and $\beta_{i\perp} = 1$. The total initial wave magnetic field energy was chosen to be 0.01 of the total initial ion perpendicular kinetic energy, and was equally distributed among the unstable modes (modes 2–21). Simulation parameters were $\omega_{ci}\Delta t = 0.077$ and $v_A\Delta t/\Delta z = 0.62$. The simulation employed 65,536 particles and 256 grid-points. In the figure $\gamma_{max} = 0.385\omega_{ci}$ is the largest of the theoretical linear mode growth rates.

by the wave [20]. When several modes are allowed by the simulation, helical momentum is no longer conserved, but the edge in velocity space is still observed. Quasilinear theory would normally applicable to the multiwave simulation, but however would not predict this type of edge structure.

Simulations were also conducted with the same bimaxwellian ion distribution and initial parameters used by Davidson and Ogden in one of their quasilinear studies [10]. The evolution of the ion temperature anisotropy $T_{i\perp}/T_{i\parallel}$ produced by each calculation is shown in Fig. 10. The initially slow relaxation of the anisotropy (for $0 \leq t < 1.2\gamma_{max}^{-1}$) occurs

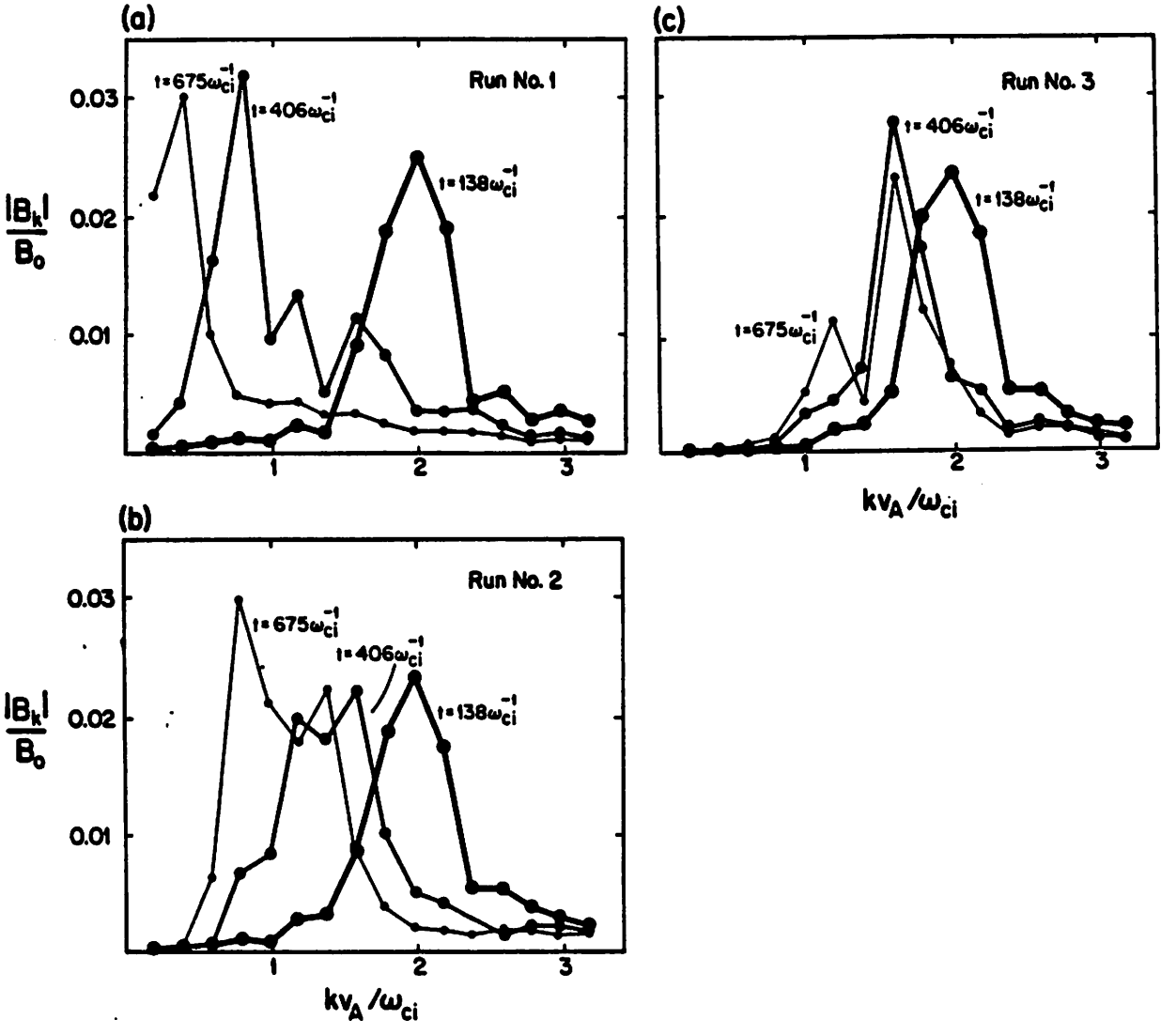

FIG. 11. Wave magnetic field mode amplitudes vs. k at times $t = 138\omega_{ci}^{-1}$, $t = 406\omega_{ci}^{-1}$, and $t = 675\omega_{ci}^{-1}$ for (a) Run No. 1, (b) Run No. 2, and (c) Run No. 3.

because the simulation was not initialized with pure eigenmodes of the AIC instability. Following this period, the simulation anisotropy histories agree fairly well. The slight differences observed in the pre-saturation relaxation rates may be due to particle trapping, the evidence for which was again observed in the simulation particle trajectories. Differences in the slower post-saturation rates might be attributable to the presence of nonlinear mode coupling in the simulation.

Differences in post-saturation behavior were also noted in the three main runs of this study. As observed in previous simulations, the temperature anisotropy $T_{i\perp}/T_{i\parallel}$ drops

rapidly during the quasilinear stage and then relaxes considerably more slowly after the instability saturates. However, as shown in Fig. 5, the slow relaxation occurs at different rates in the different runs. Differences have also been noted in the time histories of the total ion kinetic energy (Fig. 6). Curiously, the ion energy rises late in Run No. 1. Small differences also appear in the time histories of the particle and ion kinetic energy fractions in the loss region (Fig. 7(b)). Physically, we expect the differences to be attributable to the presence of nonlinear $\mathbf{E} \times \mathbf{B}$ electron drifts in Run No. 2, and to both nonlinear $\mathbf{E} \times \mathbf{B}$ electron drifts and longitudinal ion sound waves in Run No. 3. AIC wave energy may for example be transferred to sound waves via a wave-wave mode coupling process [9], and in fact longitudinal electric field energy is observed to be two orders of magnitude higher in Run No. 3 than Run No. 2.

Another feature, common among nonlinear simulations of the AIC instability [11,13] and its electron analog, the whistler instability [14], is shown in Figs. 1(a) and (b). In Run No. 1, wave magnetic field energy, primarily concentrated in the linearly most unstable

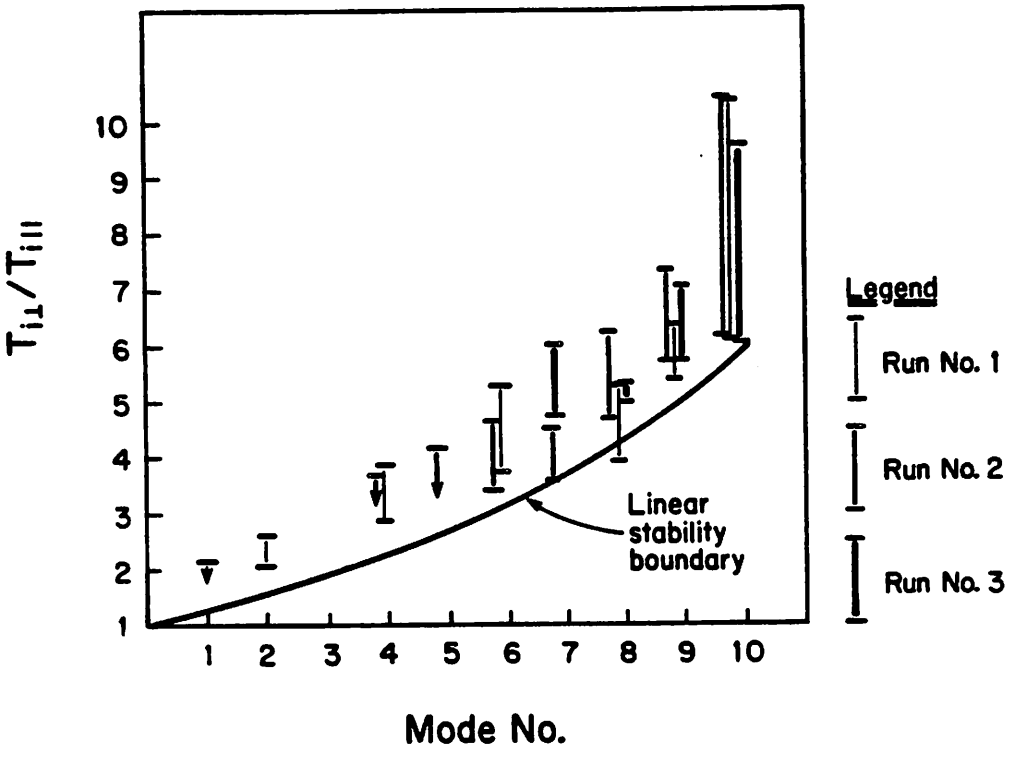

FIG. 12. Ion temperature anisotropy ($T_{i\perp}/T_{i\parallel}$) at mode saturation vs. mode number for Run Nos. 1, 2, and 3. The linear stability boundary vs. mode number assuming a bimaxwellian distribution is plotted for comparison. The stability boundary is computed from the formula [10] $kv_A/\omega_{ci} = (T_{i\perp}/T_{i\parallel} - 1)(T_{i\parallel}/T_{i\perp})^{1/2}$.

modes at saturation, is observed to transfer gradually to longer and longer wavelengths following saturation. The process occurs much more slowly in Run No. 2, and more slowly still in Run No. 3, as shown in Fig. 11. Other researchers have suggested that the shorter wavelength modes, unstable at first, give up their energy as they become linearly stable and then are damped as the ion temperature anisotropy relaxes. This theory does not explain why the long-wavelength modes, which are also linearly stable, acquire the energy, but does seem at least partially consistent with results obtained.

Figure 12 shows the ion temperature anisotropy at saturation for modes 1 through 10 in Run Nos. 1, 2, and 3. Also shown is the anisotropy present theoretically at marginal stability, assuming a bimaxwellian distribution. The two plots do not coincide—the modes saturate earlier (i.e., at higher anisotropy) than predicted—nevertheless, it is clear that the linear stability of the ion distribution plays a role in the saturation process. Early saturation is also observed by Ossakow *et al.* [14] in their simulations of the whistler instability. They suggest that the stability boundary may not be correct because the distribution at saturation may not be bimaxwellian. Our distributions do however appear to be bimaxwellian, particularly late in the runs (Figs. 3(e) and 3(f)); thus we speculate that trapping may influence saturation early in the runs, as previously indicated, while later nonlinear mode coupling is certainly present and may act to funnel away energy from otherwise unstable modes.

While the intermediate wavelength modes (i.e., the linearly unstable modes) are transferring energy to the long wavelength modes following saturation, the linearly stable, short-wavelength modes are observed to maintain a fairly constant post-saturation amplitude (Fig. 1(c)). This short-wavelength "noise" appears in all our AIC hybrid simulations, and is evidently a discrete particle effect. The short-wavelength noise level was measured in our three representative runs and also in several simulations employing bimaxwellian initial ion distributions. The results are displayed in Fig. 13. The mode magnetic field amplitudes are observed to scale as $N^{-1/2}$, where N is the number of particles, are strong functions of the initial perpendicular ion temperature, and are weak functions of the initial ion temperature anisotropy. We note that significant noise levels are even observed in Maxwellian simulations started with small perturbations. Although the distribution is theoretically stable, its particle representation is unstable due to an AIC-like mechanism acting on fine structures in the distribution [16]. The mechanism is physical and should serve as a collisionless relaxation mechanism in real plasmas. Provided with unstable transverse modes, the Maxwellian distribution eventually achieves natural noise levels in a manner entirely analogous to its non-Maxwellian counterpart.

An estimate of the noise level may be calculated using a test particle model [21]. The plasma response to the current of a test particle of surface charge density q_0/L_xL_y is

$$\frac{c}{4\pi}\nabla \times \mathbf{B} - \mathbf{J} = \frac{q_0 \mathbf{v}_0(t)}{L_x L_y}\delta(z - z_0 - v_{\|0}t), \tag{7}$$

where the 0-subscripted dynamic variables refer to the unperturbed motion of the test particle. In the spirit of the test particle model as it applies to our simulation, simulation particles double in the role of test particles; thus

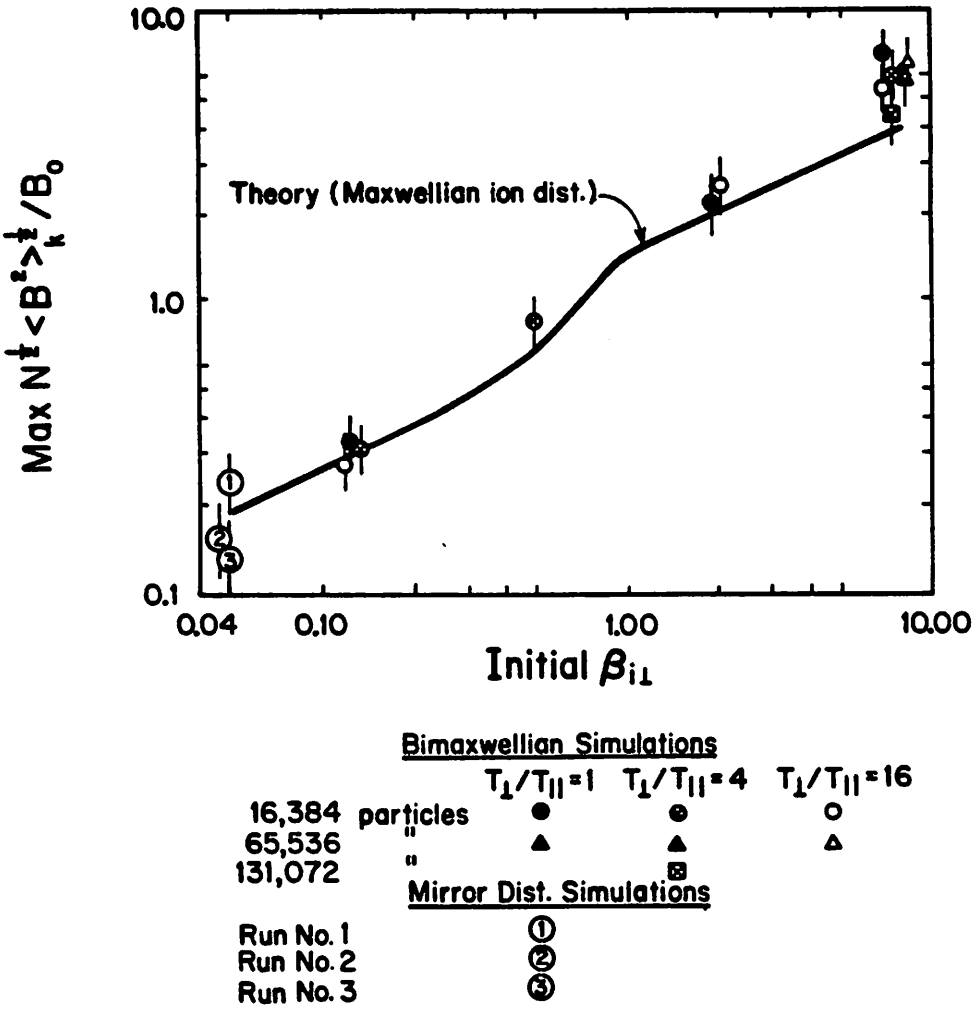

FIG. 13. Maximum short-wavelength wave magnetic field fluctuation levels, weighted by $N^{1/2}$, vs. the initial ion perpendicular beta for several bimaxwellian and mirror-distribution simulations. The theoretical dependence for a Maxwellian ion distribution is also plotted.

$$\frac{q_0}{L_x L_y} = \frac{n_0 e L_z}{N},$$

where n_0 is the number density of the plasma being simulated, L_z is the length of the simulation system, and N is the number of simulation particles. By using the linearized versions of Eqs. (1) through (4) in the left-hand side of Eq. (7), we can obtain for the magnetic field response

$$D(k, kv_{\|0} + \omega_{ci}) \frac{B^+(k,t)}{B_0} = \frac{i}{N\sqrt{2}} \frac{kv_{\perp 0}}{\omega_{ci}} e^{-i(kz_0+\theta_0)} e^{-i(kv_{\|0}+\omega_{ci})t}, \tag{8}$$

where $B^+ \equiv (B_x + iB_y)/\sqrt{2}$, θ_0 is the unperturbed gyrophase of the test particle, k is an admissible wavenumber of the system,

$$D(k,\omega) = \frac{k^2 v_A^2}{\omega_{ci}^2} + \frac{\omega}{\omega_{ci}} + \int dv_{\|}\, g(v_{\|}) \left(\frac{\omega - kv_{\|}}{\omega - kv_{\|} - \omega_{ci}} + \frac{\frac{1}{2}k^2 \langle v_\perp^2 \rangle}{(\omega - kv_{\|} - \omega_{ci})^2} \right), \tag{9}$$

is the linear dispersion function representing Eqs. (1) through (4), the ion distribution function

$$f(\mathbf{v}) = g(v_{\|}) h(v_\perp),$$

is assumed separable in $v_\perp$ and $v_{\|}$ with g and h normalized to unity, and

$$\langle v_\perp^2 \rangle \equiv \int 2\pi v'_\perp \, dv'_\perp \, v'^2_\perp h(v'_\perp).$$

Calculation of the ensemble average of $|B^+(z,t)|^2$ then yields the fluctuation magnetic field

$$\frac{\langle B_x^2(z,t) + B_y^2(z,t) \rangle}{B_0^2} = \sum_{k>0} \frac{\langle B^2 \rangle_k}{B_0^2}, \tag{10}$$

where each of the terms in the sum,

$$\frac{\langle B^2 \rangle_k}{B_0^2} = \frac{2}{N} \frac{k^2 \langle v_\perp^2 \rangle}{\omega_{ci}^2} \int dv_{\|} \frac{g(v_{\|})}{|D(k, kv_{\|} + \omega_{ci})|^2}, \tag{11}$$

includes contributions from both $\pm k$. This result is also obtained by applying the fluctuation-dissipation theorem to the linear dispersion function Eq. (9) in which $f(\mathbf{v})$ is taken to be Maxwellian.

Equation (11) has been evaluated numerically for a Maxwellian distribution, with the results plotted in Fig. 13. The noise levels obtained agree well with those observed in Maxwellian simulations. Simulations starting with non-Maxwellian distributions show short-wavelength post-saturation noise levels close to those predicted by the Maxwellian theory, even though substantial post-saturation anisotropy is generally present. Both types of simulations exhibit noise levels which scale as $N^{-1/2}$ with dependence on $\beta_{i\perp}$ matching the dependence obtained from Eq. (11).

The noise levels in our simulations were typically one order of magnitude below the longer wavelength modes of interest, and thus had little effect on these modes. This may not be true of other simulations, particularly those which employ Maxwellian ions. As we have observed, comparable noise levels persist in these simulations, and thus may be of considerable concern to other simulation studies focusing on smaller-amplitude phenomena.

IV. CONCLUSIONS

Two simulation codes have been employed in the study of the Alfvén ion-cyclotron instability, and results have been compared. We are afforded some confidence in the proper

operation of both codes as they produce identical results in the linear and quasilinear regimes. But for certain explainable discrete particle effects, both codes exhibit linear growth rates and frequencies in excellent agreement with Vlasov theory. Features of quasilinear diffusion are clearly exhibited prior to wave saturation and behave qualitatively as predicted by theory. Some ion trapping is also occurring during this phase, and may serve to explain why the simulation temperature anisotropy relaxation rate and conditions for mode saturation do not agree rigorously with quasilinear theory. Effects attributable to differences in the simulated electron physics appear following wave saturation. All runs display a slow transfer of mode energy from intermediate to long wavelengths occurring simultaneously with a gradual relaxation of the remaining anisotropy in the ion distribution function; however these processes are observed to occur at different rates in the different runs. We can speculate that the processes are slowed when additional electron physics is included because such inclusion provides additional sinks for the saturated AIC wave energy. For example, the wave energy may in part feed longitudinal ion sound waves rather than the parallel ion energy, thereby delaying the anisotropy relaxation process. We find lastly that the linearly-stable short-wavelength modes do not participate in the energy transfer process following wave saturation. Rather, these modes simply settle to thermodynamic noise levels predicted by a test-particle fluctuation model.

ACKNOWLEDGMENTS

The author wishes to thank Prof. C. K. Birdsall, Dr. B. I. Cohen, and Dr. G. R. Smith for their many ideas and thoughtful discussions. Helpful ideas and conversations were also provided by Dr. J. A. Byers and Dr. W. M. Nevins, and are gratefully acknowledged. This work was supported by U. S. Department of Energy Contract No. DE-AT03-76ET53064. Computational facilities were provided by the National Magnetic Fusion Energy Computer Center.

References

[1]B. H. Mauk and R. L. McPherron, Phys. Fluids **23**, 2111 (1980).

[2]J. M. Cornwall, F. V. Coroniti, and R. M. Thorne, J. Geophys. Res. **75**, 4699 (1970).

[3]T. A. Casper and G. R. Smith, Phys. Rev. Lett. **48**, 1015 (1982).

[4]R. P. Drake, T. A. Casper, J. F. Clauser, F. H. Coensgen, D. L. Correll, W. F. Cummins, J. C. Davis, J. H. Foote, A. H. Futch, R. K. Goodman, D. P. Grubb, R. S. Hornady, W. E. Nexsen, T. C. Simonen, and B. W. Stallard, Nucl. Fusion **21**, 359 (1981).

[5]G. R. Smith, M. J. Gerver, and T. A. Casper, Nucl. Fusion **23**, 1381 (1983).

[6]T. D. Rognlien and Y. Matsuda, Nucl. Fusion **21**, 345 (1981).

[7]Consult Ref. 18 for a list of references.

[8]G. R. Smith, W. M. Nevins, and W. M. Sharp, Phys. Fluids **27**, 2120 (1984).

[9]R. Z. Sagdeev and A. A. Galeev, *Nonlinear Plasma Theory*, edited by T. M. O'Neil and D. L. Book, (W. A. Benjamin, New York, 1969).

[10]R. C. Davidson and J. M. Ogden, Phys. Fluids **18**, 1045 (1975).

[11]T. Tajima and J. M. Dawson, Nucl. Fusion **20**, 1129 (1980).

[12]A. Hasegawa and C. K. Birdsall, Phys. Fluids **7**, 1590 (1964).

[13]S. Cuperman, A. Sternlieb, and D. J. Williams, J. Plas. Phys. **16**, 57 (1976).

[14]S. L. Ossakow, E. Ott, and I. Haber, Phys. Fluids **15**, 2314 (1972).

[15]J. A. Byers, B. I. Cohen, W. C. Condit, and J. D. Hanson, J. Comput. Phys. **27**, 363 (1978).

[16]N. F. Otani, submitted to J. Comput. Phys.

[17]D. S. Harned, J. Comput. Phys. **47**, 452 (1982).

[18]G. R. Smith, Phys. Fluids **27**, 1499 (1984).

[19]T. F. Bell, Phys. Fluids **8**, 1829 (1965).

[20]N. F. Otani, submitted to Phys. Fluids.

[21]N. A. Krall and A. W. Trivelpiece, *Principles of Plasma Physics*, 556-567 (McGraw-Hill, New York, 1973).